



Crystal facet-dependent reactivity of α - Mn_2O_3 microcrystalline catalyst for soot combustion

Li Cheng^{a,*}, Yong Men^{a,*}, Jinguo Wang^a, Hao Wang^a, Wei An^a, Yuanqiang Wang^a, Zhichen Duan^b, Jian Liu^{b,*}

^a College of Chemistry and Chemical Engineering, Shanghai University of Engineering Science, Shanghai 201620, PR China

^b State Key Laboratory of Heavy, Oil Processing, China University of Petroleum, Beijing 102249, PR China

ARTICLE INFO

Article history:

Received 27 August 2016

Received in revised form 30 October 2016

Accepted 19 November 2016

Available online 25 November 2016

Keywords:

Shape effect

α - Mn_2O_3

Oxygen activation

NO_2 formation

Soot combustion

Crystal facet-dependent reactivity

ABSTRACT

In this work, a series of α - Mn_2O_3 micro crystals with different morphologies and crystal shapes were successfully prepared by hydrothermal method and has been investigated as potential soot combustion catalysts for the first time. The activity data showed that the soot combustion efficiency were markedly affected by the shape of the prepared α - Mn_2O_3 catalysts, among which their activity ranked as α - Mn_2O_3 -cubic > α - Mn_2O_3 -truncated octahedral > α - Mn_2O_3 -octahedra. As revealed by various physicochemical characterization techniques such as XRD, SEM, HR-TEM, FT-IR, BET, H_2 -TPR, O_2 -TPD, NO- and NO + O_2 -TPSR, the enhanced activity as well as selectivity over α - Mn_2O_3 -cubic is originated with the nature of the exposed α - Mn_2O_3 (001) surface facets, on which the higher concentration of low-coordinated surface oxygen sites facilitates the oxygen activation and improves surface redox properties, thereby accelerating the formation of the crucial intermediate i.e., NO_2 formation by NO oxidation and thus promoting the overall soot combustion efficiency. Moreover, the kinetic study performed under isothermal condition provided solid evidence and proof to support that it is the exposed crystal facet, rather than surface area, to be critical to determine the catalytic performance of soot combustion. Under loose contact condition, soot combustion efficiency over best performing α - Mn_2O_3 -cubic catalyst was further enhanced in the presence of water, CO and hydrocarbons, which are essential components in real diesel exhaust. Furthermore, the cubic α - Mn_2O_3 displayed excellent durability against structural collapse upon repeated recycling test and accelerated deactivation test, demonstrating its promise for the practical use in diesel soot combustion.

© 2016 Elsevier B.V. All rights reserved.

1. Introduction

The increasingly stringent environmental legislation in many countries has led to a large amount of research on efficient elimination of diesel soot particles due to the particulate matter ($\text{PM}_{2.5}$) emitted from diesel engines contains NO_x , CO and unburned hydrocarbons, which have caused severe adverse effects to the environment and human health [1–6]. Self-regenerable soot particulate filter (SSF) has been recognized as the most readily viable technology to trap and reduce the soot emission. Arguably, one of the key challenges of using SSF technology is how to develop a high-performance catalyst that can burn soot at temperatures as low as possible to meet the temperature window (250–400 °C) of exhaust gas from diesel engine [6,7]. Although tremendous advances has been achieved for soot combustion catalysts in terms of activity

and selectivity, there is still a lot to be learned to deepen our understanding on the design principles required for a further improved soot combustion catalyst.

In recent years, the controlled synthesis of nano- or micro-sized metal oxides with different shapes and morphologies has attracted considerable research interests in the use of catalysis [8–17] and related fields [18–20]. Shape control of nano-catalyst offers great versatility in tuning the catalytic properties of a nanocrystal, especially when the surface atoms at different facets possess different activities. For instance, Shen et al. [11] reported the catalytic oxidation of CO over nano-scale catalytic particles of Co_3O_4 with a delicate control of the size and topology, and found that highly structure-ordered nano-rods of Co_3O_4 , constituting 40% of the (110) crystal plane on the nano-rod surface was able to realize a complete oxidation of CO at a temperature as low as –77 °C, showing a 10 times higher activity than those of the conventional Co_3O_4 catalysts. Trovarelli et al. [8] reported that soot combustion activity is dependent on the shape of the ceria nanoparticles, and the exposed surface. Ceria nanocubes with (100) and nanorods

* Corresponding authors.

E-mail addresses: men@sues.edu.cn (Y. Men), liujian@cup.edu.cn (J. Liu).

with (100), (110), and (111) exhibited much higher activity and conversion as compared with polycrystalline and octahedral ceria exposing mainly (111) facet. Nonetheless, it is clear that despite the significant efforts, the detailed firm evidence to unravel the origin of superior activity of ceria (100) facet was not yet provided, so that there is a need in further studies for better understanding of the shape-dependent reactivity.

Manganese oxides are widely used as efficient catalysts in many important oxidation processes such as CO oxidation [21,22], soot combustion [23,24] and total combustion of volatile organic compounds [25], due to their low cost and environmental benefits. Great efforts have been recently made to develop efficient manganese oxides catalysts for low-temperature soot combustion which have been considered as potential inexpensive alternative catalyst to precious metal for soot combustion. The outstanding performance of manganese oxide catalysts is mainly caused by enhanced redox properties and the facile redox cycle of $\text{Mn}^{2+}/\text{Mn}^{3+}$ or $\text{Mn}^{3+}/\text{Mn}^{4+}$ associated with the multi-valence $\text{Mn}^{\delta+}$ species on the surface of catalysts [26,27]. Doping of manganese oxide with alkali metal leads to pronounced improvement on surface redox properties observed as an enhanced catalytic activity in soot combustion [28].

Recently, shape-dependent catalytic behavior has been demonstrated for manganese oxides catalysts [9,29–31]. The morphology effect of manganese oxides observed in catalytic combustion was well correlated to the shape-induced facilitation of oxygen activation. Dai et al. [31] reported that the rod-like MnO_2 catalyst contained significantly more vacant oxygen sites and facile redox capability at lower temperatures, and attributed the excellent catalytic performance of $\alpha\text{-Mn}_2\text{O}_3$ nanorods to the high oxygen adsorption concentration and good low-temperature reducibility. In a very recent report [9], the different crystal shapes (cubic, truncated octahedral and octahedral) $\alpha\text{-Mn}_2\text{O}_3$ have been synthesized and applied to the catalytic degradation of phenol in aqueous solution, whose order of the catalytic efficiency is determined to be cubic > octahedral > truncated octahedral. The results of this catalytic activity was associated with exposed of different crystal facets in $\alpha\text{-Mn}_2\text{O}_3$ sample, and the catalyst with exposed (001) crystal plane showed better catalytic activity than plane (111).

Despite the efforts conducted over shape-effect of manganese oxide so far, the effect of the shape on the physicochemical and catalytic properties of manganese oxide on soot combustion remained unexplored, which hamper the understanding of the reaction mechanism and restrain our capability of rational design of high-performance catalyst with great activity and selectivity. It is anticipated that the manganese oxide species with well-controlled shape and exposed facets may lead to distinct properties and exceptional catalytic activities. For key environmental-related reaction such as soot combustion, in-depth studies of micro-crystal manganese oxide catalysts with a well-defined crystal shape and facet may provide an important insight into the structure sensitivity, allowing us to derive the design principles necessary to make better catalysts.

Herein, through a hydrothermal method, we have prepared three micro crystal $\alpha\text{-Mn}_2\text{O}_3$ catalysts with different shapes and surface facets exposed. Using these $\alpha\text{-Mn}_2\text{O}_3$ catalysts with well-defined shape as platform, we are able to study their shape-dependency in soot combustion. To the best of our knowledge, this is the first time to investigate the impact of crystal shapes and facets of manganese oxides in soot combustion. Our results revealed that cubic $\alpha\text{-Mn}_2\text{O}_3$ catalyst exhibited remarkably enhanced catalytic activity as compared with $\alpha\text{-Mn}_2\text{O}_3$ with octahedral and truncated octahedral shape, which is corroborated with the structural and chemisorptions measurements.

2. Experimental

2.1. Catalyst preparation

Three $\alpha\text{-Mn}_2\text{O}_3$ catalysts with different crystal shapes (cubic, truncated octahedral and octahedral) were prepared via a solvothermal approach with different solvents according to previously reported methodologies [9,32,33]. For $\alpha\text{-Mn}_2\text{O}_3$ -truncated octahedral, 8 mmol $\text{Mn}(\text{NO}_3)_2 \cdot 4\text{H}_2\text{O}$ was dissolved in 26 ml 2-butanol with constant stirring for 20 min to form a homogeneous solution. The solution was transferred into a 50 ml Teflon-lined stainless steel autoclave, sealed, and heated for 10 h at 120 °C. Subsequently, the autoclave was cooled to room temperature naturally. After the hydrothermal treatment, the obtained material was filtered and washed with distilled water and ethanol three or four times, then dried in air overnight at 100 °C. The $\alpha\text{-Mn}_2\text{O}_3$ -octahedral was synthesized by the same method and steps except the solvent replaced by ethanol. The $\alpha\text{-Mn}_2\text{O}_3$ -cubic was prepared via MnCO_3 which was obtained by hydrothermal methods. To prepare MnCO_3 , 6 mmol KMnO_4 and 6 mmol glucose were dissolved in 60 ml distilled water with constant stirring for 20 min to form a mixture solution and then it was transferred into a 100 ml Teflon-lined stainless steel autoclave and sealed. After that, the autoclave was heated at 150 °C for 10 h, followed by cooling, filtering, washing, and drying to obtain MnCO_3 powder. Finally, the MnCO_3 powder was calcined for 2 h at 500 °C with a heating rate of 5 °C min⁻¹ to form $\alpha\text{-Mn}_2\text{O}_3$ -cubic catalyst in air. Three $\alpha\text{-Mn}_2\text{O}_3$ catalysts with cubic, truncated octahedral and octahedral shapes were denoted as $\alpha\text{-Mn}_2\text{O}_3\text{-C}$, $\alpha\text{-Mn}_2\text{O}_3\text{-TO}$ and $\alpha\text{-Mn}_2\text{O}_3\text{-O}$, respectively.

2.2. Catalyst characterization

The crystal structure was determined by XRD (BRUKER D2 PHASER) with Cu K α radiation. The surface morphology of the catalyst was examined on a field emission-scanning electron microscopy (FESEM, Hitachi S4800) and a high-resolution transmission electron microscopy (HR-TEM, Hitachi JMF2100F). FT-IR spectra were performed on a Nicolet 380 spectrometer, and recorded from KBr pellets with the weight ratio of sample to KBr of 1/100 or by using the matched gas cell with a 10 cm length which was suitable for NO and NO₂ analysis in ambient conditions in the range of 450–4000 cm⁻¹. N₂ adsorption-desorption isotherms were performed on a Micromeritics ASAP 2460 at –196 °C, from which the surface area (S_{BET}), pore volume (V_p) and pore diameter (D_p) were calculated by applying Brunauer-Emmett-Teller (BET) and Barrett-Joyner-Halenda (BJH) models to the desorption branches. Hydrogen temperature-programmed reduction (H₂-TPR) was carried out in a Micromeritics Autochem II 2920 instrument equipped with a thermal conductivity detector (TCD) to quantify the consumed H₂. The catalysts (50 mg) were placed in a U-shaped fixed-bed quartz microreactor, pretreated in Ar atmosphere at 300 °C for 1.0 h, and then cooled to 100 °C. The pretreated catalysts were heated from 100 to 900 °C with a heating rate of 10 °C min⁻¹ under a mixture gas of 5 vol.% H₂/Ar flow (30 ml min⁻¹). Oxygen temperature-programmed desorption (O₂-TPD) were carried out in the same apparatus to H₂-TPR. Typically, 50 mg of catalysts were firstly pretreated at 500 °C with an air flow of 50 ml min⁻¹ for 30 min, cooled to 50 °C, and then exposed to pure He for 5.0 min, lastly heated up to 900 °C with a heating rate of 10 °C min⁻¹. The released O₂ was determined by TCD. The temperature-programmed surface reaction with NO and O₂ (NO + O₂-TPSR) experiments were carried out in a fixed-bed tubular quartz system (Φ = 6.0 mm). 100 mg catalyst was placed in the fixed-bed and pretreated for 1 h at 500 °C in 10% O₂ then cooled to 100 °C. The reactant gases were composed of 5000 ppm NO and

5 vol.% O₂ balanced with He and the reaction temperature ranged from 100 to 700 °C with a heating rate of 5.0 °C min⁻¹. The effluent gases were monitored by a mass spectrometer and the mass number (*m/z*) of 30 and 46 were used for monitoring NO and NO₂, respectively. In order to investigate the impact of surface reactive oxygen species on the formation of NO₂, the temperature programmed surface reaction of NO (NO-TPSR) experiments was also conducted under the same conditions as NO + O₂-TPSR but only 1% NO in the reactant gases balanced with He.

2.3. Catalytic activity measurement

The catalytic performances of all the α-Mn₂O₃ catalysts were evaluated with a temperature-programmed oxidation reaction (TPO) on a fixed-bed tubular quartz system ($\Phi = 6.0$ mm) and each TPO ran from 200 to 700 °C with a heating rate of 2.0 °C min⁻¹. In order to accurate control the reaction temperature, a K-type thermocouple was placed in the center of the tube furnace to obtain a good contact with the catalytic bed. The catalyst 100 mg and soot 10 mg (MA100 Mitsubishi, Japan) were mixed with a spatula lasting for five minutes in order to reproduce the loose contact conditions [7,24,34,35]. In the catalytic tests, the mixture of the catalyst should be pretreated for 30 min at 200 °C in nitrogen to eliminate the influence of other impurities. The reactant gases containing 5 vol.% O₂ and 0.25 vol.% NO balanced with N₂ were mixed uniformly then passed through the mixture of the catalyst at a flow rate of 80 ml/min and the GHSV (Gas Hourly Space Velocity) is 9990 h⁻¹. The effluent CO and CO₂ coming from the reactor were analyzed by an on-line automobile emission analyzer (HPC500). For investigating the effect of water vapor (10 vol.% H₂O), deionized water was delivered by a syringe pump into an evaporator (200 °C) to generate water vapor which was then carried into the reactor by the flowing carrier gases. A cold trap was installed before the gas analyzer to condense moisture in the effluent gas. The catalytic performance of catalysts was evaluated by the values of *T_m*, which was defined as the temperature at which CO₂ content reach the maximum during the TPO measurement. The selectivity to CO₂ formation (*S_{CO2}*) was defined as the CO₂ outlet concentration (*C_{CO2}*) divided by the sum of the CO₂ and CO outlet concentrations; i.e., $S_{CO2} = C_{CO2} / (C_{CO} + C_{CO2})$. And the *S_{CO2}^m* was denoted as the *S_{CO2}* at the *T_m*. In order to ensure the reliability of the results, the reproducibility of all the activity tests was checked by repeating each result at least three times and found to be within acceptable limits (± 2 °C). To gain more accurate kinetic values, the kinetic study was performed under isothermal condition of different temperatures at a higher gas flow rate (160 ml/min) and low soot conversion (<12%) to ensure the catalyst works in the kinetic regime. The feed composition used was the same as the TPO reaction.

3. Models and computational details

All calculations were performed by using the spin-polarized periodic density functional theory (DFT) [36,37]. The electron-ion interactions were described by using projector augmented wave (PAW) [38,39] method. The generalized gradient approximation (GGA) was used with the exchange-correlation functional of Perdew-Burke-Ernzerhof (PBE) [40]. The Kohn-Sham orbitals are expanded in a plane-wave basis set with a kinetic energy cutoff of 400 eV. The conjugate gradient algorithm was used in optimization in which the convergence threshold was set to be 10–4 eV in total energy and 0.02 eV/Å in Hellmann-Feynman force on each atom. The Brillouin-zone was sampled by $4 \times 4 \times 1$ k-points using the Monkhorst-Pack scheme [41]. We employed the GGA + U approach with *U* = 2.8 eV and *J* = 1.2 eV for strongly localized Mn 3d electrons [42] to correctly address the electronic structure of α-Mn₂O₃,

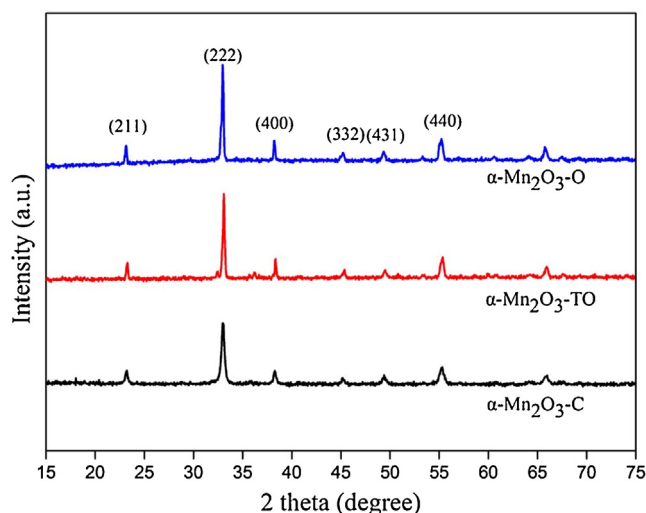


Fig. 1. XRD patterns of different α-Mn₂O₃ catalysts.

particularly important for defective O-vacancy site of transition metal oxide [43].

The α-Mn₂O₃ unit cell was modeled based on the bixbyite crystal structure (lattice constants: *a* = 9.4157 Å; *b* = 9.4233 Å; *c* = 9.4047 Å) reported in the literature [44]. We built 7-layer *p*(1 × 1) Mn₂O₃ (001) and 9-layer *p*(1 × 1) Mn₂O₃ (111) slab having O-terminated surface on both top and bottom layer for calculations of formation energy of surface oxygen vacancy (*O_v*) on different facets of nanoparticle, which correspond to 1/12ML (i.e., total 12 surface O atoms on each surface) of *O_v* on the surface. A vacuum layer of 12 Å was adopted along the “*Z*” direction to avoid the artificial interactions between the slab and its periodic images. Initial *O_v*-configurations were created by removing one of the O-h or O-l atoms on the surface. During geometry optimization, the top O-Mn-O layer of slab was only allowed to relax while the rest of atoms were fixed in their bulk positions. The formation energies of oxygen vacancy were calculated by using the formula:

$$\Delta E = E(\text{slab}(O_v)) + \frac{1}{2} * E(O_2) - E(\text{slab}).$$

Where *E* represents the total energy of slab with one oxygen vacancy, gas-phase O₂, and the perfect slab. More negative values denote thermodynamically more favorable process for oxygen vacancy formations.

4. Results and discussion

4.1. Structural and morphological characterization of catalysts

The crystalline structure of manganese oxides catalysts was examined by XRD. The diffraction profiles for these three catalysts are displayed in Fig. 1. It can be seen the three catalysts exhibited the same characteristic diffraction peaks as in literature [9], which can be indexed to (211), (222), (400), (332), (431) and (440) planes, corresponding to 2θ of 23.1 °C, 33.0 °C, 38.2 °C, 45.2 °C, 49.3 °C, 55.2 °C, according to pure cubic bixbyite α-Mn₂O₃ structure (JCPDS # 41-1442). No other impurities were identified from the diffractograms of XRD.

FESEM analyses were carried out on three fresh α-Mn₂O₃ catalysts to characterize their morphology, as presented in Fig. 2, α-Mn₂O₃-C showed well-defined and regular cubic shapes with slightly rounded edges and corners at an edge length of 0.8–2 μm. The other two samples displayed clear octahedral and truncated octahedral shapes with sharp edges, which contained

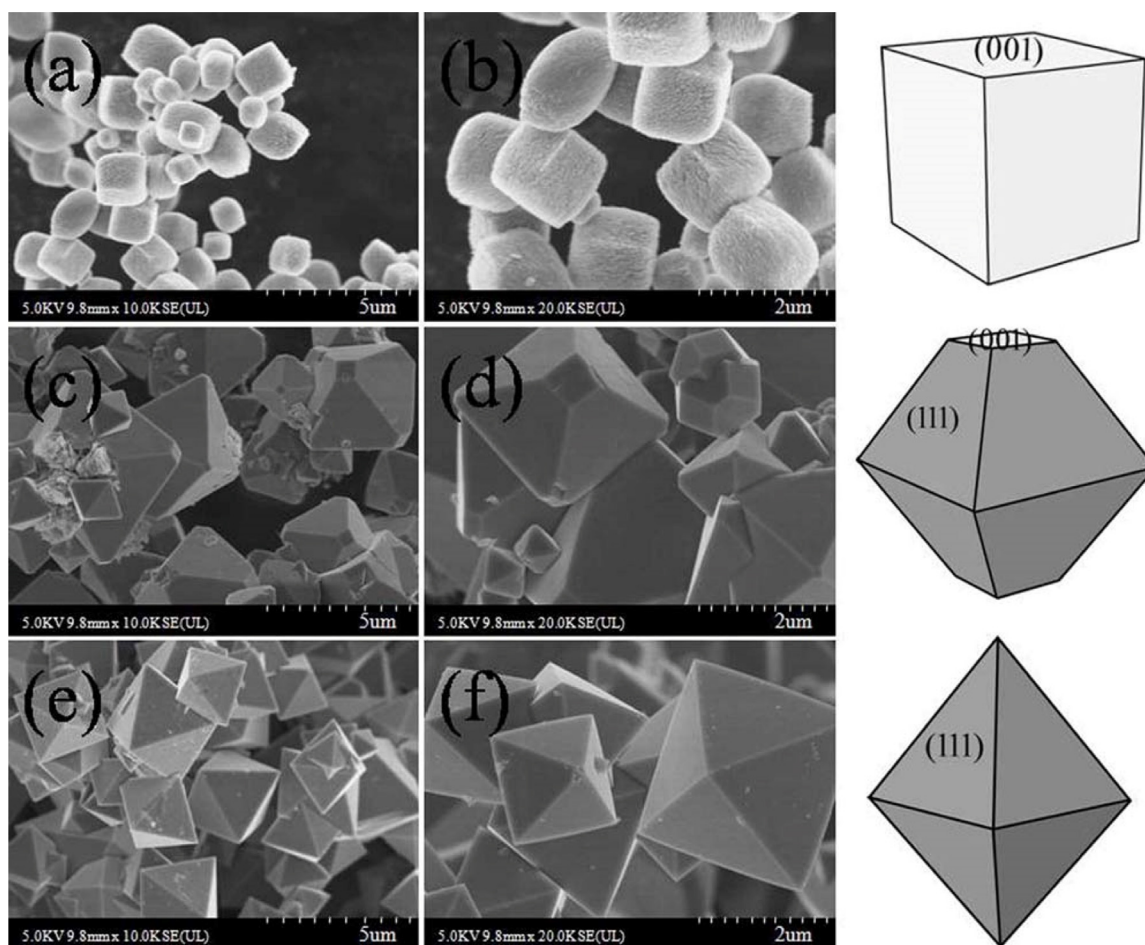


Fig. 2. FESEM images of different α - Mn_2O_3 catalysts: (a, b) α - Mn_2O_3 -C, (c, d) α - Mn_2O_3 -TO and (e, f) α - Mn_2O_3 -O.

predominant micro crystal phase plus minor small aggregates. The size of α - Mn_2O_3 -O and α - Mn_2O_3 -TO micro crystal was ca. 0.5–2.5 μm and 1–2.5 μm , respectively. The SEM results demonstrate that the preparation conditions have a significant influence on the morphologies of the α - Mn_2O_3 samples, in good accordance with previous results [9,32]. According to Li et al. [9,32], such control over the morphology led to α - Mn_2O_3 with the different exposed crystal planes due to the different growth rate of (001) and (111) facet. As a result, α - Mn_2O_3 -C and α - Mn_2O_3 -O predominantly exposed their (001) and (111) crystal facets, respectively, whereas α - Mn_2O_3 -TO afforded the exposure of mixed (001) and (111) facets. Their shape-dependent structure models are displayed in Fig. 2.

Some more details about the morphologies and crystallographic features of the various Mn_2O_3 products were obtained by using TEM techniques. From TEM images of Fig. 3(A–C), one can find the consistent size distribution of cubic Mn_2O_3 , the octahedral and truncated octahedral with the results of SEM. The HR-TEM analysis offered more solid proofs for the formation of three Mn_2O_3 micro crystals with well-defined shapes and exposed crystal facets. The insets of Fig. 3 show the high resolution images with the structurally uniformed lattice fringes. The interplanar spacing of α - Mn_2O_3 -C is determined to be 0.23 nm which corresponds to the (004) plane of cubic α - Mn_2O_3 . And the (004) planes is exactly parallel to the (001) planes which means the α - Mn_2O_3 -C mainly exposed the (001) crystal facet. The lattice fringe spacing of α - Mn_2O_3 -O is 0.27 nm corresponding to the (222) plane of octahedral Mn_2O_3 . And the (222) facet stays exactly parallel to the (111) facet which indicates the α - Mn_2O_3 -OT mainly exposed (111) crystal facet. The α - Mn_2O_3 -TO showed the same interplanar results as α - Mn_2O_3 -O because

only (111) crystal facet of α - Mn_2O_3 -TO can be visualized by HR-TEM while the (001) facet can hardly be probed due to a relatively larger thickness of this orientation.

Fig. 4 presents the FT-IR spectra of different α - Mn_2O_3 catalysts. All samples showed five features at 3438, 1636, 665, 572 and 524 cm^{-1} in the same position. These three peaks (665, 572 and 524 cm^{-1}) at lower wave number were assigned to stretching vibration of Mn–O–Mn bond presenting in α - Mn_2O_3 [45,46]. The broad absorption band (3438 cm^{-1}) in the higher energy region was attributed to the O–H stretching vibration which was caused by the adsorbed moisture on the surface of α - Mn_2O_3 samples and the peaks at 1636 cm^{-1} may be also caused by water [46,47]. No other impurities were found on α - Mn_2O_3 samples by using FT-IR.

The N_2 adsorption-desorption isotherms and BJH pore size distributions of three α - Mn_2O_3 catalysts were displayed in Fig. 5 and the data was summarized in Table 1. Fig. 4 displays that three catalysts all exhibited the typical type IV N_2 adsorption-desorption isotherms with H3 hysteresis loop in the relative pressure (P/P_0) range from 0.6 to 1.0. Meanwhile, their corresponding pore size distribution curves demonstrated the wide pore size range from micropore to mesopore. The maximum pore sizes of α - Mn_2O_3 -C, α - Mn_2O_3 -TO and α - Mn_2O_3 -O are 21.0, 4.0, and 2.0 nm respectively. From Table 1, one can see the α - Mn_2O_3 -C has the largest surface area of 30.3 m^2/g while the other two have very smaller surface area of 2.5 m^2/g and 1.0 m^2/g for α - Mn_2O_3 -TO and α - Mn_2O_3 -O, respectively, which is consistent to the results of FESEM. The smaller surface area and pore volume of the latter two samples obtained from N_2 adsorption are mainly attributed to interparticles apertures, which are observed usually as mesopores.

Table 1
Physicochemical parameters and catalytic soot combustion efficiencies of different α - Mn_2O_3 catalysts.

Catalysts	S_{BET} (m^2/g)	V_p (cm^3/g)	D_p (nm)	H_2 consumption (mmol/g)	O_2 desorption (mmol/g)	T_m ($^\circ\text{C}$)	$S^m_{\text{CO}_2}$ (%)
α - Mn_2O_3 -C	30.3	0.197	20.9	6.2	0.34	435	96.3
α - Mn_2O_3 -TO	2.5	0.008	13.4	6.1	0.33	494	89.7
α - Mn_2O_3 -O	1.0	0.003	13.9	6.1	0.33	540	85.2

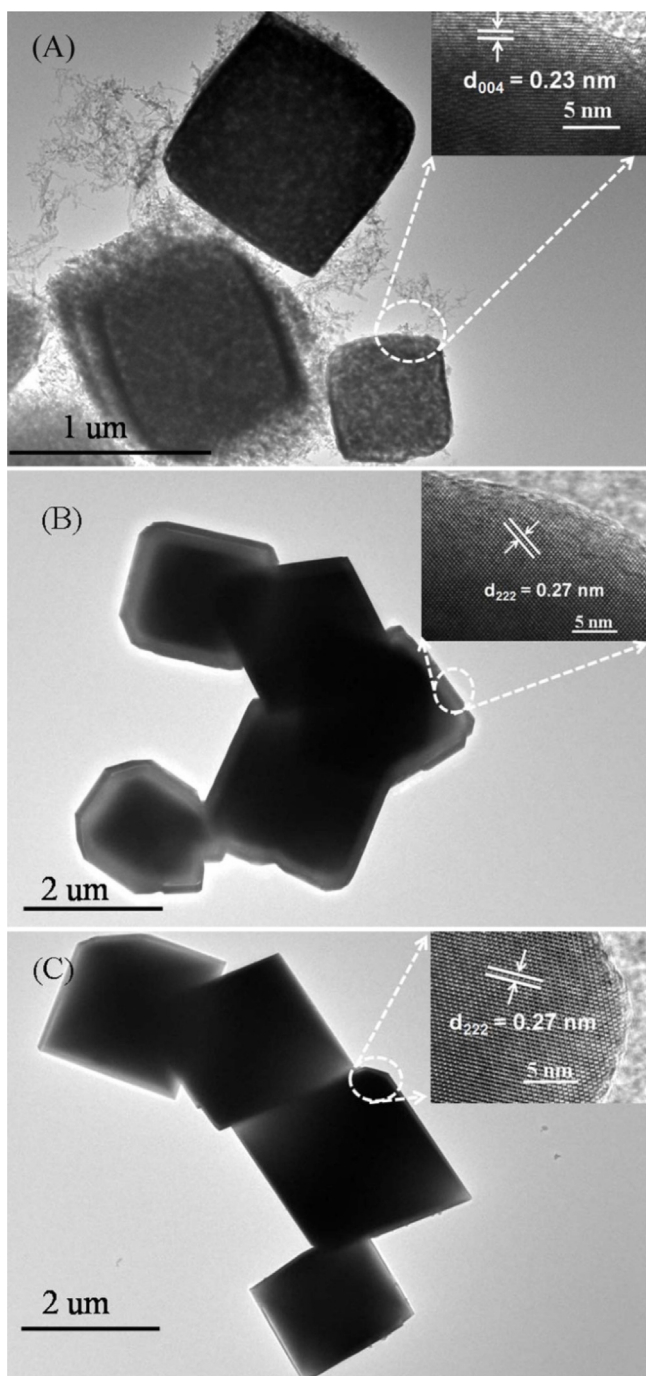


Fig. 3. TEM and HRTEM images of different catalysts: (A) α - Mn_2O_3 -C, (B) α - Mn_2O_3 -TO and (C) α - Mn_2O_3 -O.

4.2. Surface chemical properties

Fig. 6A illustrates the H_2 -TPR profiles of the as-prepared catalysts. It can be observed that the three α - Mn_2O_3 samples showed different reduction profiles by interaction with H_2 . For the

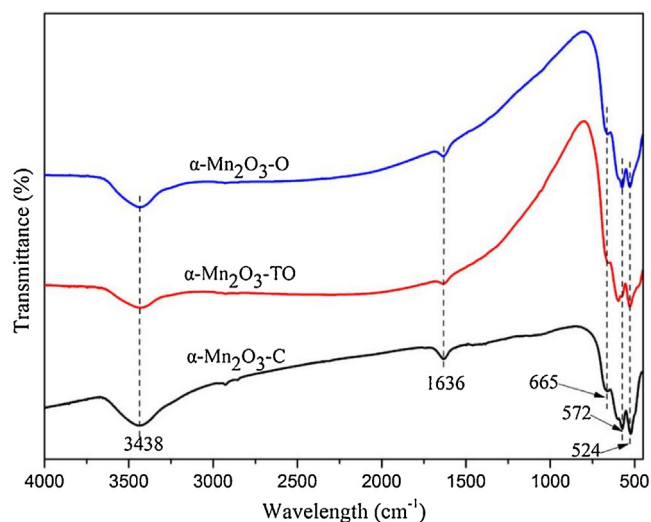


Fig. 4. FTIR spectra of different α - Mn_2O_3 catalysts.

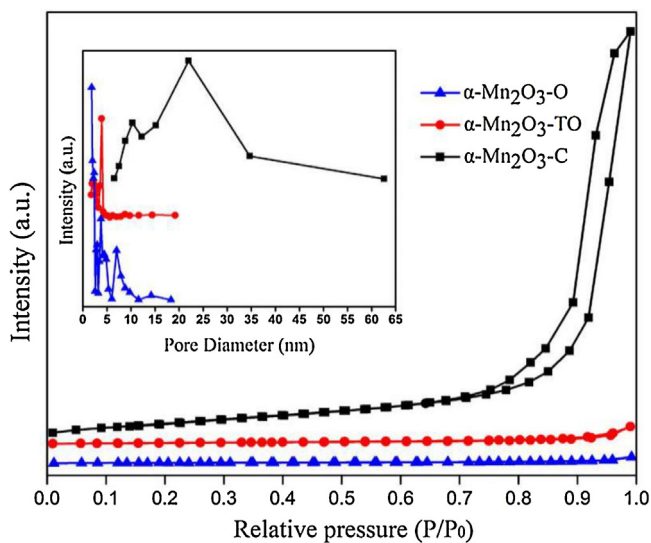


Fig. 5. N_2 adsorption-desorption isotherms and the pore size distribution curves of different α - Mn_2O_3 catalysts.

α - Mn_2O_3 -C sample, there are two strong reduction peaks centered at 280°C and 390°C , respectively. In contrary, a weak reduction peak at 260°C and a strong reduction peak at 490°C were identified over α - Mn_2O_3 -TO. In case of α - Mn_2O_3 -O, low temperature reduction feature disappeared and a main reduction peak at 490°C was found together with a shoulder peak at 420°C . According to the previous results [48–51], the reduction process could be reasonably divided into two stepwise reductions. The formation of the relatively weak reduction peak at low temperature and the main reduction peak at higher temperature was attributed to the stepwise transformation of $\text{Mn}_2\text{O}_3 \rightarrow \text{Mn}_3\text{O}_4 \rightarrow \text{MnO}$ under H_2 atmosphere. Based on the consumed H_2 , the reduced degree of Mn_2O_3 is estimated to be 32.6%, in good agreement with the stepwise reduction of Mn_2O_3 to MnO . Although the three

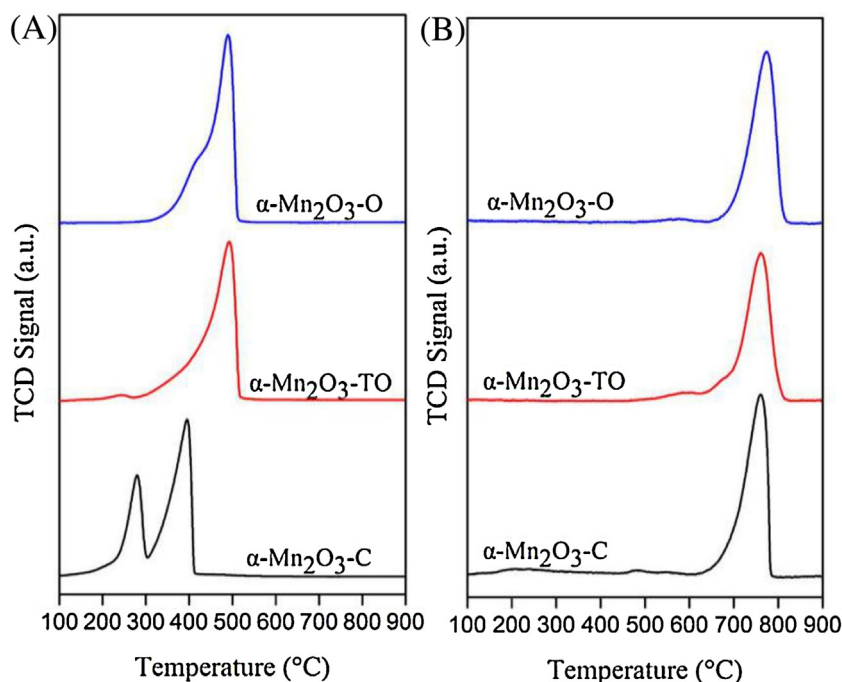


Fig. 6. H_2 -TPR (A) and O_2 -TPD (B) profiles of different $\alpha\text{-Mn}_2\text{O}_3$ catalysts.

$\alpha\text{-Mn}_2\text{O}_3$ catalysts consumed the quite close H_2 during TPR test, it can be clearly seen the reducibility of these three catalysts followed a shape-dependent consequence, i.e., $\alpha\text{-Mn}_2\text{O}_3\text{-C} > \alpha\text{-Mn}_2\text{O}_3\text{-TO} > \alpha\text{-Mn}_2\text{O}_3\text{-O}$. The result of O_2 -TPD was shown Fig. 6B. It can be seen that three $\alpha\text{-Mn}_2\text{O}_3$ samples all exhibited an obvious desorption peak at around 750°C which is attributed to β -oxygen species associated with lattice oxygen [50]. Noticeably, nearly all oxygen in O_2 -TPD were released above 700°C , i.e., beyond the maximum operation temperature of soot combustion test. It has been well known that the oxygen species may have different reactivity under different conditions e.g. in the purging of inert gas, for instance in O_2 -TPD, or in the presence of a reducer such as H_2 , NO and soot. Kureti et al. [52,53] reported the insignificant thermal release of oxygen occurred in the absence of the reducer during O_2 -TPD, but the presence of the reducing agent soot facilitated the release and uptake of oxygen by the catalyst at lower temperatures. Hence, the lattice oxygen released in H_2 -TPR and at high temperatures in O_2 -TPD may also take part in the soot combustion in the presence of a reducer (soot and NO).

H_2 -TPR has provided a great deal of practical information on the interaction of H_2 and $\alpha\text{-Mn}_2\text{O}_3$ catalyst surface, and also offered valuable information of surface structure and exposed planes from the onset of reduction peak. However, the information is indirect as to how strongly the lattice oxygen is held in the $\alpha\text{-Mn}_2\text{O}_3$ catalysts. A much more direct measure would be using the probe molecules actually involved in soot combustion. Therefore, NO-TPSR and NO + O_2 -TPSR were performed to investigate the chemical reactivity on catalyst surface.

As depicted in Fig. 7, NO-TPSR illustrated that $\alpha\text{-Mn}_2\text{O}_3$ catalysts with different shapes and exposed facets showed very different capability for NO_2 ($m/z=46$) generation via NO oxidation by surface active oxygen species. The NO_2 ($m/z=46$) peak of $\alpha\text{-Mn}_2\text{O}_3\text{-C}$ detected by means of online MS was significantly larger than that of $\alpha\text{-Mn}_2\text{O}_3\text{-TO}$ and $\alpha\text{-Mn}_2\text{O}_3\text{-O}$, which could be associated with the difference of specific surface area between these samples. Aside from the NO_2 intensity, it is important to note that reactivity of surface oxygen species to oxidize NO decreased in the sequence of $\alpha\text{-Mn}_2\text{O}_3\text{-C} > \alpha\text{-Mn}_2\text{O}_3\text{-TO} > \alpha\text{-Mn}_2\text{O}_3\text{-O}$, in consistent with

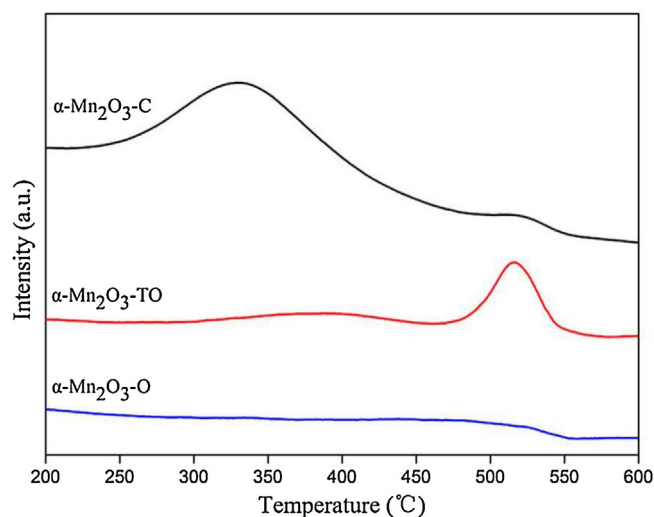


Fig. 7. Shape-dependent NO-TPSR profiles.

H_2 -TPR results. The results demonstrated that the $\alpha\text{-Mn}_2\text{O}_3\text{-C}$ with surface facet (001) afforded the most abundant surface reactive oxygen species for NO oxidation.

The results of NO + O_2 -TPSR for three $\alpha\text{-Mn}_2\text{O}_3$ catalysts were shown in Fig. 8A. In the coexistence of gaseous NO and O_2 , a strong shape-dependency of NO oxidation was also observed, similar to the results obtained from NO-TPSR. The NO_2 signal over $\alpha\text{-Mn}_2\text{O}_3\text{-O}$ increased with rising temperature until the thermodynamic equilibrium ($\text{NO} + \text{O}_2 \rightarrow \text{NO}_2$) was attained at about 420°C , and started to decrease with increasing temperature, mainly due to the unfavorable formation of NO_2 at higher temperatures governed by the thermodynamic restriction [54]. In comparison, $\alpha\text{-Mn}_2\text{O}_3\text{-TO}$ was more effective for NO oxidation, approaching the equilibrium at 395°C . The $\alpha\text{-Mn}_2\text{O}_3\text{-C}$ is unarguably the best performing catalyst for NO oxidation, allowing the attainment of thermodynamic equilibrium at much lower temperature of 330°C . The NO oxidation capability was ranked as the order of $\alpha\text{-Mn}_2\text{O}_3\text{-C} > \alpha\text{-Mn}_2\text{O}_3\text{-TO} > \alpha\text{-Mn}_2\text{O}_3\text{-O}$.

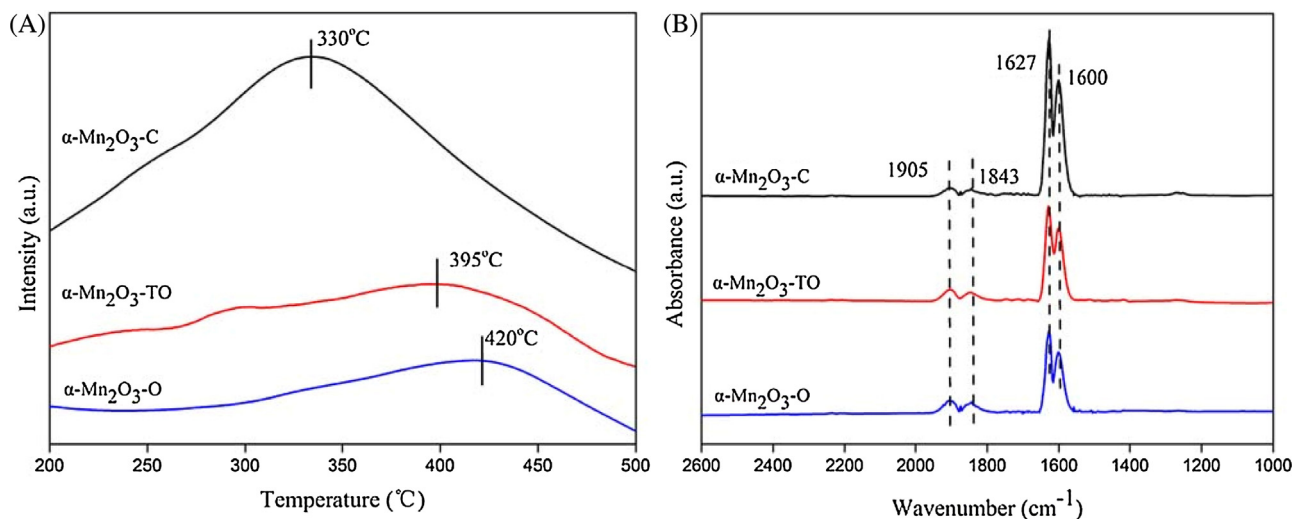


Fig. 8. Shape-dependent NO + O₂-TPSR profiles (A) and in-situ IR spectra (B).

Mn₂O₃-TO > α -Mn₂O₃-O, agreeing well with the sequence of the H₂-TPR and NO-TPSR results. The difference in reactivity for NO oxidation was double checked by gas composition monitored by in-situ IR method conducted at 280°C. Fig. 8B shows that the absorption band strength at 1627 and 1600 cm⁻¹ assignable to NO₂ obviously followed the same trend of α -Mn₂O₃-C > α -Mn₂O₃-TO > α -Mn₂O₃-O, reconfirming the shape-dependent NO oxidation reactivity.

4.3. Shape-dependent reactivity of α -Mn₂O₃ on soot combustion

The activities of three α -Mn₂O₃ samples for soot combustion were evaluated by TPO method which was conducted on a fixed-bed tubular quartz system under the conditions of 5 vol.% O₂ and 0.25 vol.% NO balanced with N₂ and the results were listed in Table 1 and Fig. 9. The strong shape-dependency in terms of activity (T_m) and CO₂ selectivity ($S^{m}_{CO_2}$) was observed over the α -Mn₂O₃ samples with three different shapes. The T_m and $S^{m}_{CO_2}$ over α -Mn₂O₃-O were determined to be 540°C and 85.2%. By tuning the shape of α -Mn₂O₃ samples into truncated octahedral, soot combustion efficiency was significantly improved both with respect to activity and selectivity, exhibiting the T_m and $S^{m}_{CO_2}$ value of 494°C and 89.3%, respectively. The activity of α -Mn₂O₃-C catalyst was further

enhanced with the shape of cube, presenting the T_m of 435°C and the $S^{m}_{CO_2}$ of 96.3%. Clearly, the soot combustion efficiency both in terms of activity and selectivity are in the order of α -Mn₂O₃-C > α -Mn₂O₃-TO > α -Mn₂O₃-O.

Shape is one typical parameter for tailoring the properties of a micro/nano-crystal-based material. In the literatures [8–10], the shape-dependent catalytic behavior for micro/nano-catalysts is often correlated with their preferential or selective exposed crystal facets. The shape controls the exposed facets and thus surface structure of a micro/nano-crystal, as well as surface atom arrangement and coordination. As such, shape control offers a great versatility in tuning the catalytic properties of a micro/nano-crystal, especially when the surface atoms at different facets possess different reactivities. In particular, for the shape-dependent catalysis of manganese oxides, Li et al. [9] have shown that octahedral Mn₂O₃ exhibited higher activity catalytic activity than truncated octahedral Mn₂O₃ in pyridoin transformation to quinoxaline. Very recently, by investigating a set of micro crystal α -Mn₂O₃ samples with different shapes, Wang et al. [9] have concluded that cubic α -Mn₂O₃ with predominant (001) facet exhibited a superior activity as compared with truncated octahedral α -Mn₂O₃ with (001)&(111), and octahedral α -Mn₂O₃ with (111) for catalytic degradation in aqueous solution, which was mainly associated with its surface atom

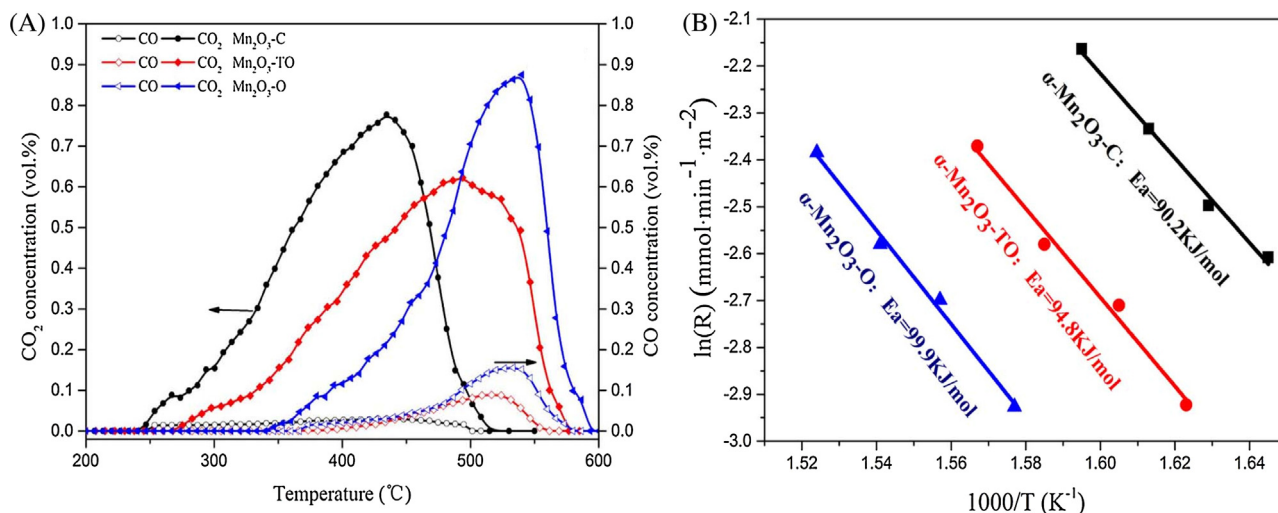


Fig. 9. Soot combustion efficiency over different α -Mn₂O₃ catalysts on the same mass basis (A) and Arrhenius-type plot of reaction rates of different α -Mn₂O₃ catalysts (B).

Table 2The normalized soot conversion rates of different α -Mn₂O₃ catalysts.

Catalysts	Temperature (°C)	mol s ⁻¹ m ⁻² × 10 ⁻¹⁰	Temperature (°C)	mol s ⁻¹ m ⁻² × 10 ⁻¹⁰
α -Mn ₂ O ₃ -C	320	2.69	354	6.38
α -Mn ₂ O ₃ -TO	321	1.89	358	4.19
α -Mn ₂ O ₃ -O	325	1.72	361	3.01

arrangement. However, the root cause for the greater reactivity of octahedral α -Mn₂O₃ with (111) over truncated octahedral α -Mn₂O₃ with mixed (001) and (111) was not provided. Very likely, the observed reactivity difference in our case was due to their different kinetic relevance of crystal facet-dependent effect in both reactions.

Surface lattice oxygen and oxygen vacancies are always involved in oxidation reactions catalyzed by manganese oxides-based catalysts; therefore, improving the reactivity of surface lattice oxygen and the population of oxygen vacancy in α -Mn₂O₃ is the key to optimize the catalytic activity. The facet-dependent activity of soot combustion has been confirmed over ceria by Trovarelli et al. [8], which demonstrated that the soot combustion is a surface-dependent reaction sensitively to the exposed crystal facet. Indeed, our results demonstrated that controlling the shape of α -Mn₂O₃ catalysts offers a very useful tool in tailing their reactivity and selectivity for soot combustion, in accordance with Trovarelli's work. By varying the shape of α -Mn₂O₃, a chemically more favorable (001) surface facet may be exposed, thus influencing the catalytic behavior. The α -Mn₂O₃ with three different shapes and exposed facets consumed similar amounts of hydrogen during the stepwise reduction of Mn₂O₃ to MnO, however, the reduction temperature follow the order of α -Mn₂O₃-C > α -Mn₂O₃-TO > α -Mn₂O₃-O. The catalytic combustion efficiency of the various α -Mn₂O₃ followed the same sequence, which correlated well to the surface reducibility and reactivity of surface lattice oxygen. Detailed structural analyses confirmed that α -Mn₂O₃-C catalyst with exposed (001) facet contained more abundant reactive oxygen species and facile redox properties at lower reaction temperatures, which facilitated NO/O₂ activation and promoted formation of the presumed key intermediate, i.e., NO₂.

Notably, activity data in Fig. 9 were obtained by performing TPO test over the catalyst with the same mass basis but with different specific surface area at the mean time. The influence of specific

surface area is generally accounted for their catalytic behavior in such typical gas-solid-solid reaction. Therefore, in order to effectively rule out the impact of surface area, the isothermal kinetic study of soot combustion has been performed at very low conversion within kinetic-relevant regime to derive the kinetic relevant data and reaction rate normalized to per unit specific surface area, as it has been done in reference [8]. In order to calculate the activation energy more accurately, the values of the apparent activation energy (*E_a*) is calculated from Arrhenius-type plot of reaction rates of different α -Mn₂O₃ catalysts under the low conversion rate of soot combustion (<12%). Fig. 9B shows that α -Mn₂O₃-O, α -Mn₂O₃-TO and α -Mn₂O₃-C has activation energy of 99.9 kJ/mol, 94.8 kJ/mol and 90.2 kJ/mol, respectively. The lower the *E_a* value is, the easier the soot can be oxidized [55–57]. The catalytic activities increased in the sequence of α -Mn₂O₃-O < α -Mn₂O₃-TO < α -Mn₂O₃-C while the activation energy follows the reversed order. Therefore, the impact of surface area was effectively ruled out by this isothermal kinetic study. The kinetic results provided the direct evidence that it is the exposed crystal facet, rather than surface area, to be critical to determine the catalytic performance of soot combustion. And the quantified values of the reaction rate at two different temperatures in Table 2 also show clearly the superior performance of crystal facet (001).

The results presented here showed clear and firm evidences of the effect of surface facet exposure in the reactivity of α -Mn₂O₃ for soot combustion. To gain further insight into the origin of difference on facet-dependent reactivity, the optimized surface atomic configurations in the (001) and (111) of α -Mn₂O₃ unit cell were modeled and displayed in Fig. 10. One can see that prominent surface reconstruction occurs for both (001) and (111) facets, where the corresponding C_{2v} and C_{3v} symmetry are collapsed completely after the optimization, resulting in extremely rough surface. On (001) facet, 36% of the 2-coordinated surface O atoms are turned into 1-coordinated surface O atoms (i.e., O-l), while on

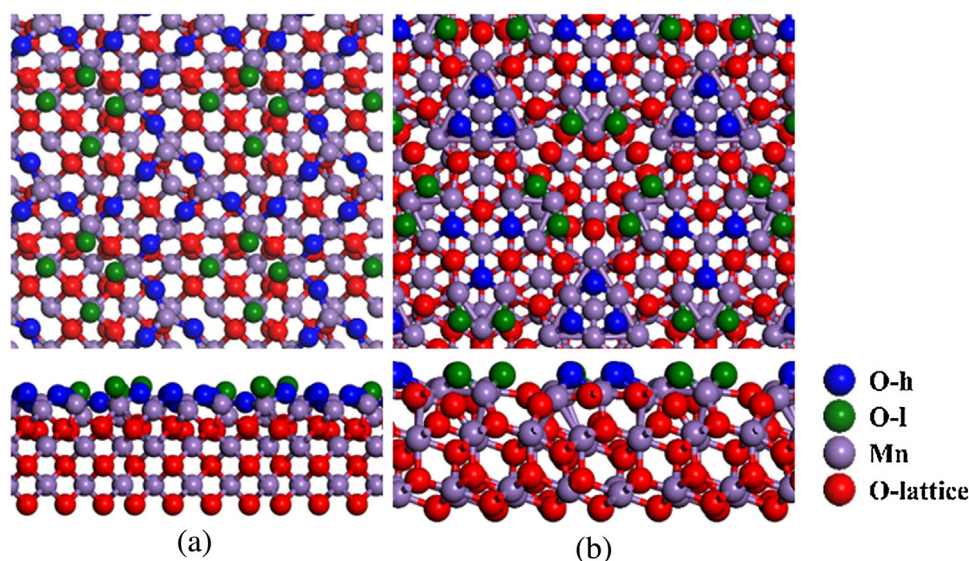


Fig. 10. Atomic arrangement of optimized α -Mn₂O₃ (001) and (111) surface. (a) (001) facet, (b) (111) facet. Top view and side view are shown in upper and lower panel, respectively. O-h: surface O atoms of high-coordination number; O-l: surface O atoms of low-coordination number; O-lattice: O atoms in lattice.

Table 3

Calculated formation energy (in eV) for 1/12 ML of oxygen vacancy (O_V) from removal of high-coordination (O-h) and low-coordination (O-l) O atoms on α - Mn_2O_3 surface.

Surface	O-l	O-h
Mn_2O_3 (001)	−1.03	1.17
Mn_2O_3 (111)	1.68	2.09

(111) facet, 50% of the 3-coordinated surface O atoms are turned into 2-coordinated surface O atoms (i.e., O-l). Interestingly, surface O atoms on (001) facet are found to be flexible in that one sub-layer O atom is able to move up to top-layer position meanwhile two top-layer O atoms are able to move down to sub-layer position after optimization. In stark contrast, no such exchanges are observed from (111) facet. As is known that reactivity of surface O atoms are critically dependent on their coordination number (CN) or state [58], it's therefore expected (001) facet is more reactive than (111) facet in terms of redox capability. Indeed, our calculated formation energies of oxygen vacancy clearly point to such a trend. As shown in Table 3, O_V -formation energy for O-l (CN = 1) and O-h (CN = 2) on (001) facet is −1.03 eV and 1.17 eV, respectively, while O_V -formation energy for O-l (CN = 2) and O-h (CN = 3) on (111) facet is 1.68 eV and 2.09 eV, respectively. This demonstrate that two kinds of surface O atoms on (001) facet, even those from sub-layers or bulk due to its high flexibility, are energetically more facile to be released participating in soot combustion reaction than those on (111) facet, also supporting our H_2 -TPR and NO-TPSR results that more H_2 or NO consumption is observed from (001) facet than (111) facet at lower onset temperature. Moreover, DFT calculation results have important implication that energetically the gaseous oxygen can be more facily activated on (001) facet to account for our crystal facet dependent NO + O_2 -TPSR and soot combustion reactivity. Accordingly, the soot combustion can be accelerated by exposing more (001) facets of α - Mn_2O_3 .

4.4. The effect of feed composition on soot combustion

Since real diesel exhaust may constitute a very complicated mixture of H_2O , CO_x , NO_x and HC (hydrocarbons) under the working condition of diesel engine, understanding the impact of these molecules on combustion efficiency is of both practical and fundamental significance. The α - Mn_2O_3 -C catalyst was chosen for the purpose. The soot combustion was also conducted in the different feed compositions using the same TPO procedure and the results were presented in Fig. 11.

As shown in Fig. 11A, the T_m was determined to be 558 °C in the presence of oxygen in the feed gases, whereas the T_m value was shift down to 435 °C in the coexistence of NO and O_2 , implying that NO participates very actively in the catalysis cycle of soot combustion, which is fully consistent with the so-called “NO₂-assisted mechanism” proposed in the literatures [5,59,60]. NO-TPSR and NO + O_2 -TPSR results can also be rationalized by this mechanism which hypothesizes NO₂, the molecule with much stronger oxidation capability, to be the key intermediate in promoting the oxidation of carbon soot. The reactivity order of α - Mn_2O_3 -C > α - Mn_2O_3 -TO > α - Mn_2O_3 -O could be well understood by their shape- or facet-dependent NO oxidation capability.

The reaction rate of soot combustion in the presence of 10 vol% H_2O was much faster than the corresponding value in the absence of H_2O , an indicative of great enhancement of H_2O in combustion efficiency, in accordance with the previous reports [60,61]. For instance, Burachaloo et al. [60] suggested that OH radicals generated from O atoms and H_2O molecules in the discharge facilitate the re-oxidization of the metal oxide vacancies generated by the consumption of oxygen, thus favoring the enhancement of the soot oxidation efficiency. Uchisawa et al. [61] proposed that water vapor play a role in facilitating the decomposition of the highly stable carbon surface species formed by the partial oxidation of the reacting carbon surface by NO₂-attack.

The results shown in Fig. 11B indicate the beneficial effect of 1 vol.% CO and 0.85 vol.% hydrocarbons in the feed stream on the soot combustion efficiency while the introducing 2.5 vol.% CO_2 in the feed has no influence on soot combustion. This result is encouraging and practically important for the design and development of α - Mn_2O_3 -based combustion catalysts since H_2O , CO and hydrocarbons are in the permanent presence of real diesel exhausts. Nevertheless, further study is needed in order to gain deeper insight of the beneficial role of different reactants in soot combustion, which is apparently out of the scope of this work.

4.5. The stability test of α - Mn_2O_3 -cubic catalyst

In order to determine the reusability of micro crystal α - Mn_2O_3 catalyst, the catalytic stability of the α - Mn_2O_3 catalyst with cubic shape was tested by consecutive TPO measurements under the same reaction conditions. As can be seen from Fig. 12, the α - Mn_2O_3 -C catalyst exhibited no appreciable deactivation after 4 times of recycling with almost unchanged T_m and $S^m_{CO_2}$, demonstrating its outstanding stability. The crystal and morphological structure of α - Mn_2O_3 -C catalyst examined remained intact after 4 times of

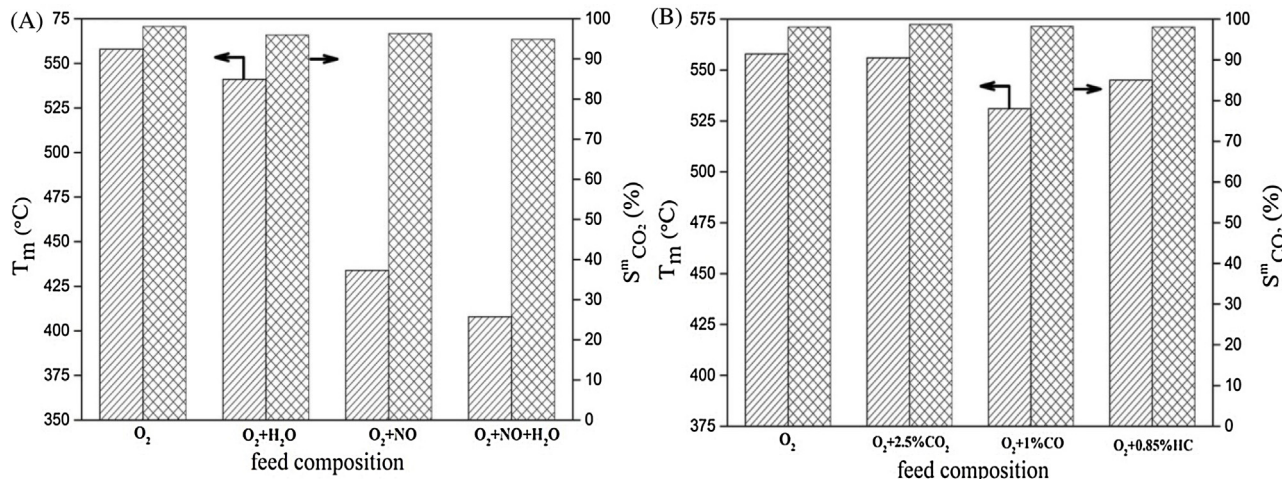


Fig. 11. The effect of NO and H_2O (A), CO_x and HC (B) on soot combustion efficiency over α - Mn_2O_3 -C catalyst.

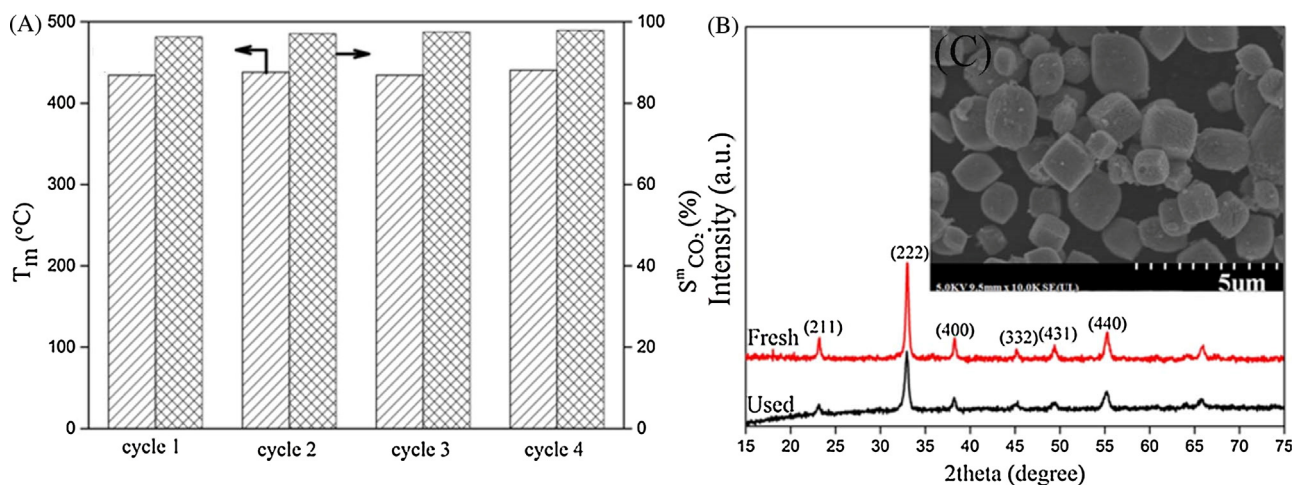


Fig. 12. The stability test of α - Mn_2O_3 -C catalyst (A), XRD patterns (B) and FESEM images (C, inset for used catalyst) of fresh and used α - Mn_2O_3 -C catalysts.

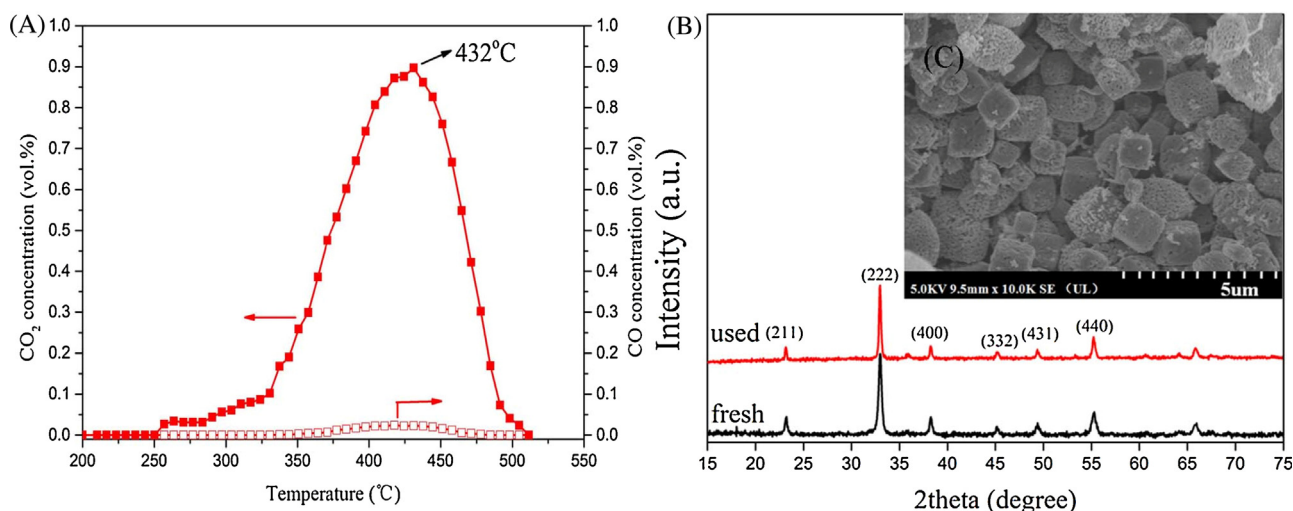


Fig. 13. The accelerated deactivation test of soot combustion over α - Mn_2O_3 -C catalyst (A), XRD patterns (B) and FESEM images (C, inset for used catalyst) of fresh and used α - Mn_2O_3 -C catalysts.

TPO cycles can be observed from Fig. 13, as evidenced by XRD and FESEM, suggesting that α - Mn_2O_3 -C catalyst exhibited excellent catalytic stability in the soot combustion and met the needs required for practical reuses in soot combustion catalysts.

To further examine the thermal stability, the accelerated deactivation test was investigated on α - Mn_2O_3 -C catalyst which was pretreated in water vapor for 4 h at 850 °C and further treated with a standard soot TPO. As shown in Fig. 13A, the α - Mn_2O_3 -C after being treated under harsh condition exhibited the almost the same catalytic activity for soot combustion compared with the one treated by the standard procedure. Fig. 13B shows the nearly same XRD pattern after accelerated deactivation test of the spent α - Mn_2O_3 -C catalysts as the pattern on fresh one. Furthermore, the FESEM inset after the accelerated deactivation test in Fig. 13C demonstrates that the sample preserved its original morphology, an indicative of the excellent thermal stability of α - Mn_2O_3 -C.

5. Conclusions

Three α - Mn_2O_3 catalysts with different micro crystal shapes were successfully prepared by hydrothermal method and their shape-control reactivity was evaluated in diesel soot combustion. The α - Mn_2O_3 -C catalyst with cubic shape was observed to

have the superior catalytic performance as compared with the α - Mn_2O_3 catalysts of truncated octahedral and octahedral shape. The shape-dependent reactivity of α - Mn_2O_3 were correlated with their different redox properties and chemical natures which are originated from the extent of exposed (001) facets of for the three catalysts, as supported by the isothermal kinetic study and HR-TEM. As revealed by H_2 -TPR, NO-TPSR, and $\text{NO} + \text{O}_2$ -TPSR, the superior reactivity of (001) facet was corroborated with the good low temperature reducibility, abundant low-coordinated surface active O species, high ability to activate O_2 as well as NO molecules, and NO_2 -promoted mechanism. Furthermore, cubic α - Mn_2O_3 exhibited excellent both structural and activity stability after 4 runs of recycling tests and accelerated deactivation test. These results showed that micro crystal α - Mn_2O_3 with different shapes may act as a very useful platform to bridge gap between model surface and practical catalysts, and to provide the insights required for developing a high-performance real soot combustion catalysts.

Acknowledgements

This work is supported by the Program for Professor of Special Appointment (Eastern Scholar) at Shanghai Institutions of Higher Learning, National Natural Science Foundation of China (Grant

21503133, 21673137, 21673290 and 21376261), Natural Science Foundation of Shanghai City (16ZR1413900, 15ZR1419100), the Scientific Research Foundation for the Returned Overseas Chinese Scholars from State Education Ministry, Municipal Education of Shanghai (ZZGCD15031), Zhanchi Plan (nhrc-2015-12), Task-based Knowledge Innovation Team (2014td16 and 2016td03) and Startup Foundation (2015-20 and 2014-01) of Shanghai University of Engineering Science.

References

- [1] A. Bueno-López, *Appl. Catal. B* 146 (2014) 1–11.
- [2] B. Frank, M.E. Schuster, R. Schlogl, D.S. Su, *Angew. Chem. Int. Ed.* 52 (2013) 2673–2677.
- [3] M. Ammann, M. Kalberer, D.T. Jost, L. Tobler, E. Rössler, D. Piguet, H.W. Gaggeler, U. Baltensperger, *Nature* 395 (1998) 157–160.
- [4] M. Matti Maricq, *J. Aerosol Sci.* 38 (2007) 1079–1118.
- [5] S. Liu, X. Wu, D. Weng, M. Li, R. Ran, *ACS Catal.* 5 (2015) 909–919.
- [6] R. Kimura, J. Wakabayashi, S.P. Elangovan, M. Ogura, T. Okubo, *J. Am. Chem. Soc.* 130 (2008) 12844–12845.
- [7] Y. Wei, Z. Zhao, J. Liu, S. Liu, C. Xu, A. Duan, G. Jiang, *J. Catal.* 317 (2014) 62–74.
- [8] E. Aneggi, D. Wiater, C. de Leitenburg, J. Llorca, A. Trovarelli, *ACS Catal.* 4 (2014) 172–181.
- [9] E. Saputra, S. Muhammad, H. Sun, H.-M. Ang, M.O. Tade, S. Wang, *Appl. Catal. B* 154 (2014) 246–251.
- [10] Z. Wu, M. Li, S.H. Overbury, *J. Catal.* 285 (2012) 61–73.
- [11] X. Xie, Y. Li, Z.Q. Liu, M. Haruta, W. Shen, *Nature* 458 (2009) 746–749.
- [12] Z. Hu, X. Liu, D. Meng, Y. Guo, Y. Guo, G. Lu, *ACS Catal.* (2016) 2265–2279.
- [13] H. Mistry, A.S. Varela, S. Köhl, P. Strasser, B.R. Cuenya, *Nature* (2016) 16009.
- [14] Y. Li, W. Shen, *Chem. Soc. Rev.* 43 (2014) 1543–1574.
- [15] K. Zhou, Y. Li, *Int. Ed. Angew. Chem.* 51 (2012) 602–613.
- [16] J. González-Prior, R. López-Fonseca, J.I. Gutiérrez-Ortiz, B. de Rivas, *Appl. Catal. B* 199 (2016) 384–393.
- [17] F. Petronella, M.L. Curri, M. Striccoli, E. Fanizza, C. Mateo-Mateo, R.A. Alvarez-Puebla, T. Sibillano, C. Giannini, M.A. Correa-Duarte, R. Comparelli, *Appl. Catal. B* 178 (2015) 91–99.
- [18] J.B. Fei, Y. Cui, X.H. Yan, W. Qi, Y. Yang, K.W. Wang, Q. He, J.B. Li, *Adv. Mater.* 20 (2008) 452–456.
- [19] X. Xiao, X. Liu, H. Zhao, D. Chen, F. Liu, J. Xiang, Z. Hu, Y. Li, *Adv. Mater.* 24 (2012) 5762–5766.
- [20] J. Wang, P. Rao, W. An, J. Xu, Y. Men, *Appl. Catal. B* 195 (2016) 141–148.
- [21] L.-C. Wang, Q. Liu, X.-S. Huang, Y.-M. Liu, Y. Cao, K.-N. Fan, *Appl. Catal. B* 88 (2009) 204–212.
- [22] L. Liu, X. Gu, Y. Cao, X. Yao, L. Zhang, C. Tang, F. Gao, L. Dong, *ACS Catal.* 3 (2013) 2768–2775.
- [23] I. Atribak, A. Bueno-López, A. García-García, P. Navarro, D. Frías, M. Montes, *Appl. Catal. B* 93 (2010) 267–273.
- [24] J. Wang, G. Yang, L. Cheng, E.W. Shin, Y. Men, *Catal. Sci. Technol.* 5 (2015) 4594–4601.
- [25] X. Tang, J. Li, L. Sun, J. Hao, *Appl. Catal. B* 99 (2010) 156–162.
- [26] P. Legutko, P. Stelmachowski, M. Trębala, Z. Sojka, A. Kotarba, *Top. Catal.* 56 (2013) 489–492.
- [27] P. Sudarsanam, B. Hillary, M.H. Amin, S.B.A. Hamid, S.K. Bhargava, *Appl. Catal. B* 185 (2016) 213–224.
- [28] P. Legutko, T. Jakubek, W. Kaspara, P. Stelmachowski, Z. Sojka, A. Kotarba, *Catal. Commun.* 43 (2014) 34–37.
- [29] K. Selvakumar, S.M. Senthil Kumar, R. Thangamuthu, G. Kruthika, P. Murugan, *Int. J. Hydrogen Energy* 39 (2014) 21024–21036.
- [30] Z.Y. Fei, B. Sun, L. Zhao, W.J. Ji, C.T. Au, *Chem. Eur. J.* 19 (2013) 6480–6487.
- [31] F. Wang, H. Dai, J. Deng, G. Bai, K. Ji, Y. Liu, *Environ. Sci. Technol.* 46 (2012) 4034–4041.
- [32] W.-N. Li, L. Zhang, S. Sithambaram, J. Yuan, X.-F. Shen, M. Aindow, S.L. Suib, *J. Phys. Chem. C* 111 (2007) 14694–14697.
- [33] S. Lei, K. Tang, Z. Fang, Q. Liu, H. Zheng, *Mater. Lett.* 60 (2006) 53–56.
- [34] Y. Wei, Z. Zhao, T. Li, J. Liu, A. Duan, G. Jiang, *Appl. Catal. B* 146 (2014) 57–70.
- [35] X. Zhou, H. Chen, G. Zhang, J. Wang, Z. Xie, Z. Hua, L. Zhang, J. Shi, *J. Mater. Chem. A* 3 (2015) 9745–9753.
- [36] G. Kresse, J. Furthmüller, *Phys. Rev. B* 54 (1996) 11169–11186.
- [37] G. Kresse, J. Hafner, *Phys. Rev. B* 47 (1993) 558–561.
- [38] P.E. Blochl, *Phys. Rev. B* 50 (1994) 17953–17979.
- [39] G. Kresse, D. Joubert, *Phys. Rev. B* 59 (1999) 1758–1775.
- [40] J.P. Perdew, K. Burke, M. Ernzerhof, *Phys. Rev. Lett.* 77 (1996) 3865–3868.
- [41] H.J. Monkhorst, J.D. Pack, *Phys. Rev. B* 13 (1976) 5188–5192.
- [42] A.I. Liechtenstein, V.I. Anisimov, J. Zaanen, *Phys. Rev. B* 52 (1995) R5467.
- [43] W. An, *Phys. Chem. Chem. Phys.* 17 (2015) 22529–22532.
- [44] S. Geller, *Acta Crystallogr. Sect. B: Struct. Sci* 27 (1971) 821–828.
- [45] Y. Ding, C. Hou, B. Li, Y. Lei, *Electroanal.* 23 (2011) 1245–1251.
- [46] S. Gnanam, V. Rajendran, *J. Sol-Gel Sci. Technol.* 58 (2010) 62–69.
- [47] S. Chen, F. Liu, Q. Xiang, X. Feng, G. Qiu, *Electrochim. Acta* 106 (2013) 360–371.
- [48] M.R. Morales, B.P. Barbero, L.E. Cadús, *Appl. Catal. B* 74 (2007) 1–10.
- [49] E.R. Stobbe, B.A. De Boer, J.W. Geus, *Catal. Today* 47 (1999) 161–167.
- [50] J.R. Paredes, E. Díaz, F.V. Díez, S. Ordóñez, *Energy Fuels* 23 (2009) 86–93.
- [51] Y.F. Han, F. Chen, Z. Zhong, K. Ramesh, L. Chen, E. Widjaja, *J. Phys. Chem. B* 110 (2006) 24450–24456.
- [52] S. Wagloehner, J.N. Baer, S. Kureti, *Appl. Catal. B* 147 (2014) 1000–1008.
- [53] S. Wagloehner, S. Kureti, *Appl. Catal. B* 125 (2012) 158–165.
- [54] Y. Wei, J. Liu, Z. Zhao, A. Duan, G. Jiang, *J. Catal.* 287 (2012) 13–29.
- [55] X. Yu, J. Li, Y. Wei, Z. Zhao, J. Liu, B. Jin, A. Duan, G. Jiang, *Ind. Eng. Chem.* 53 (2014) 9653–9664.
- [56] Z. Li, M. Meng, Y. Zha, F. Dai, T. Hu, Y. Xie, J. Zhang, *Appl. Catal. B* 121–122 (2012) 65–74.
- [57] L.F. Nascimento, P.C. d. SousaF Filho, J.F. Lima, O.A. Serra, *J. Braz. Chem. Soc.* 26 (2015) 1315–1320.
- [58] W. An, A.E. Baber, F. Xu, M. Soldemo, J. Weissnrieder, D. Stacchiola, P. Liu, *ChemCatChem* 6 (2014) 2364–2372.
- [59] D. Fino, N. Russo, G. Saracco, V. Specchia, *J. Catal.* 242 (2006) 38–47.
- [60] H. Ranji-Burachaloo, S. Masoomi-Godarz, A.A. Khodadadi, Y. Mortazavi, *Appl. Catal. B* 182 (2016) 74–84.
- [61] A.O.J. Oi-Uchisawa, A. Ogata, R. Enomoto, S. Kushiya, *Appl. Catal. B* 21 (1999) 9–17.